Showcasing research from Dr Xueliang (Andy) Sun's Nanomaterials and Energy Group at Western University, Canada (http://www.eng.uwo.ca/people/asun/default.htm).

Title: LiFePO$_4$–graphene as a superior cathode material for rechargeable lithium batteries: impact of stacked graphene and unfolded graphene

LiFePO$_4$ nanoparticles are uniformly dispersed and tightly anchored to the unfolded graphene network, resulting in a high discharge capacity of 166.2 mA h g^{-1} (98% of the theoretical capacity). Image depicts the LiFePO$_4$ particles anchored to the crimped unfolded graphene.

As featured in:
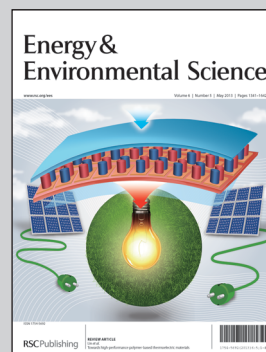
See Sun *et al.*,
Energy Environ. Sci., 2013, **6**, 1521.

PAPER

LiFePO₄–graphene as a superior cathode material for rechargeable lithium batteries: impact of stacked graphene and unfolded graphene†

Jinli Yang,[a] Jiajun Wang,[a] Yongji Tang,[a] Dongniu Wang,[ab] Xifei Li,[a] Yuhai Hu,[a] Ruying Li,[a] Guoxian Liang,[c] Tsun-Kong Sham[b] and Xueliang Sun*[a]

In this work, we describe the use of unfolded graphene as a three dimensional (3D) conducting network for LiFePO₄ nanoparticle growth. Compared with stacked graphene, which has a wrinkled structure, the use of unfolded graphene enables better dispersion of LiFePO₄ and restricts the LiFePO₄ particle size at the nanoscale. More importantly, it allows each LiFePO₄ particle to be attached to the conducting layer, which could greatly enhance the electronic conductivity, thereby realizing the full potential of the active materials. Based on its superior structure, after post-treatment for 12 hours, the LiFePO₄–unfolded graphene nanocomposite achieved a discharge capacity of 166.2 mA h g⁻¹ in the 1st cycle, which is 98% of the theoretical capacity (170 mA h g⁻¹). The composite also displayed stable cycling behavior up to 100 cycles, whereas the LiFePO₄–stacked graphene composite with a similar carbon content could deliver a discharge capacity of only 77 mA h g⁻¹ in the 1st cycle. X-ray absorption near-edge spectroscopy (XANES) provided spectroscopic understanding of the crystallinity of LiFePO₄ and chemical bonding between LiFePO₄ and unfolded graphene.

Broader context

In order to relieve the pressure from limited fossil fuels and increasing environmental and global warming issues, intensive studies have been focused on the development of alternative renewable and clean energy sources. Lithium ion batteries (LIBs) have been regarded as a promising energy storage system for applications in electric and hybrid electric vehicles after two decades of development. Polyanion typed cathode material LiFePO₄ has attracted the most interest because of its environmental benignity, high safety and theoretical capacity. However, the major limitation for LiFePO₄ is its intrinsically poor conductivity, which could be overcome by highly conductive hybrid structures with carbon coating or graphene incorporation. In this paper, we present the use of unfolded graphene as a three dimensional (3D) conducting network for LiFePO₄ nanoparticle growth. The facile designed hybrids exhibit both high specific capacity and rate performances benefiting from application of the unfolded graphene matrix, which serves as a conducting 3D nano-network, enabling both Li⁺ and electrons to migrate and reach each of these LiFePO₄ particles, hence realizing the full potential of the active materials.

Introduction

The use of lithium ion batteries (LIBs) for electrical vehicles (EVs) and hybrid electrical vehicles (HEVs) has been pursued in an attempt to displace fossil fuel and address environmental issues.[1–3] Cost, lifetime and safety are the major issues in the successful application of LIBs for electrical energy storage involved in transportation.[4,5] Moreover, the high storage performance of electrical energy at high charge and discharge rates is essential for EVs and HEVs.[6] LiFePO₄ (LFP) has attracted the most interest because of its environmental benignity, high safety, acceptable operating voltage (3.4 V *vs.* Li⁺/Li), and reasonable theoretical capacity of 170 mA h g⁻¹.[7] However, the challenge for the application of LFP in EVs and HEVs is the sluggish diffusion of lithium ions and the poor electrical conductivity of LFP (∼10⁻⁹ S cm⁻¹).[8] To overcome the ionic and electronic transport limitations, a variety of methods have been attempted, including metal doping,[9,10] surface coating or admixing with electronically conductive materials,[11–16] and controlling the particle size.[17,18] Of these methods, carbon coating and conductive additives are the most effective and facile for improving the conductivity of LFP.[12,13] However, uniform coating on LFP is difficult to achieve,[19,20] so the electrode performance is limited in terms of rate capability and lifetime.

[a] Department of Mechanical and Materials Engineering, University of Western Ontario, London, ON, N6A 5B9 Canada. E-mail: xsun@eng.uwo.ca; Tel: +1 519 661-2111 ext. 87759

[b] Department of Chemistry, University of Western Ontario, London, ON, N6A 5B7 Canada

[c] Clariant (Canada), 1475, rue Marie-Victorin, St-Bruno, QC, J3V 6B7 Canada

† Electronic supplementary information (ESI) available: Experimental part, TGA curves of LFP–UG and LFP–SG composites, and HRTEM and SAED of LFP–UG composites annealed at 2 h, 6 h and 24 h. See DOI: 10.1039/c3ee24163g

To enhance the performance of the electrode materials, graphene has recently been used as a 3D conducting matrix to grow and anchor insulating materials because of its superior conductivity, high mechanical strength, structural flexibility, and more importantly, high surface area (theoretical value of $2630~m^2~g^{-1}$).[21–23] Therefore, the application of 2D graphene nanosheets to allow the effective use of the active materials is essential in high-power batteries.

Some recent studies have focused on graphene-modified LFP. Ding *et al.* fabricated a LFP–graphene composite using a co-precipitation method.[24] In their work, the graphene suspension was prepared first, followed by the addition of a precursor into the solution, and finally the graphene-modified LFP was obtained by post-heat treatment. However, there were some unattached and aggregated LFP particles in the composites. In this case, the unattached LFP was not sufficiently utilized, thereby resulting in a limited enhancement of the specific capacity. Su *et al.* mechanically mixed graphene with LFP particles. This method did not adequately combine LFP and graphene because the graphene was not well dispersed, resulting in limited utilization of the LFP active material ($150~mA~h~g^{-1}$ at 0.1 C).[25] Our previous work also investigated graphene-modified LFP in which graphene nanosheets were used as a 3D network to incorporate LFP particles, and this modification improved the performance of the composite ($146~mA~h~g^{-1}$ at 0.1 C).[26] The wrinkled graphene nanosheets were distributed uniformly into the LFP particles. However, on a large scale, the stacked graphene nanosheets only combined in a limited way with LFP.

Based on the above studies, only the surface portion of the stacked graphene nanosheets can be used to increase the electronic conductivity, as the interior layers were not utilized. In addition, the unattached LFP particles were not sufficiently used during cycling.[26] Compared with stacked graphene, unfolded graphene possesses fewer layers and is smaller, allowing a more uniform dispersion of the $LiFePO_4$ precursor and a larger contact area between the graphene and the LFP active material and thereby full utilization of the unfolded graphene. In addition, unfolded graphene, which has a higher surface area than the stacked graphene, provides more nucleation sites[22,23] to anchor LFP nuclei, further restricting the size and agglomeration of the LFP particles.

In this paper, we applied unfolded graphene as a conducting matrix in order to sufficiently utilize the LFP active materials. To demonstrate good dispersion of LFP on the unfolded graphene, stacked graphene was used for comparison. Unfolded graphene improved the dispersion and greatly enhanced the utilization of LFP in comparison with stacked graphene nanosheets. Nano-sized LFP particles were dispersed uniformly and tightly anchored to the unfolded graphene network, whereas larger sized (micro-scale) LFP particles were loosely attached on the stacked graphene. Furthermore, the unfolded graphene matrix acted as a 3D network, enabling Li^+ and electrons to migrate and reach each LFP particle and resulting in a high discharge capacity of $166.2~mA~h~g^{-1}$, which is close to the theoretical capacity. Various advanced characterization techniques, including field-emission scanning electron microscopy (SEM),

transmission electron microscopy (TEM), high-resolution TEM (HRTEM), X-ray diffraction (XRD), Raman and synchrotron analysis, were used to understand and explain the results.

Results and discussion

The stacked graphene was prepared by thermal reduction of graphene oxide, whereas unfolded graphene was synthesized by hydrazine reduction of graphene oxide in solution (detailed procedure is described in the ESI†).[27–29] The $LiFePO_4$–unfolded graphene (LFP–UG) and $LiFePO_4$–stacked graphene (LFP–SG) nanocomposites were obtained by a facile method combining a sol–gel route and a solid-state reaction approach.

Typical SEM and TEM images of stacked graphene and unfolded graphene are shown in Fig. 1. From low magnification micrographs (Fig. 1a and c), the stacked graphene consists of multiple flakes that are closely packed in the perpendicular direction to the basal plane of graphene sheets. These closely packed flakes make the size of stacked graphene up to 10 μm, whereas the size of the unfolded graphene is approximately 500 nm, which is 20 times smaller than that of stacked graphene. In addition, the unfolded graphene has fewer flakes than the stacked graphene. TEM images (Fig. 1b and d) clearly reveal the difference in morphology. The stacked graphene has multiple wrinkled layers, whereas the unfolded graphene exhibits an even and flat structure with individual flake, resulting in a higher surface-to-volume ratio.

The LFP–SG and LFP–UG composites were obtained by adding the same amount of dispersed stacked graphene or unfolded graphene suspension to the $LiFePO_4$ precursor solution. The final products were collected after calcination of the dried xerogel.

SEM and TEM images of the LFP–SG and LFP–UG composites are shown in Fig. 2. Micro-scale LFP particles were obtained when stacked graphene was used, and only a few LFP
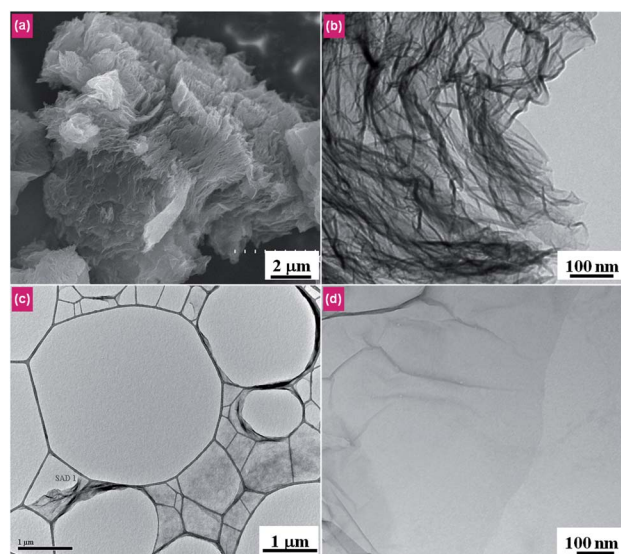

Fig. 1 (a) SEM image and (b) TEM image of stacked graphene, (c) and (d) TEM images of unfolded graphene.
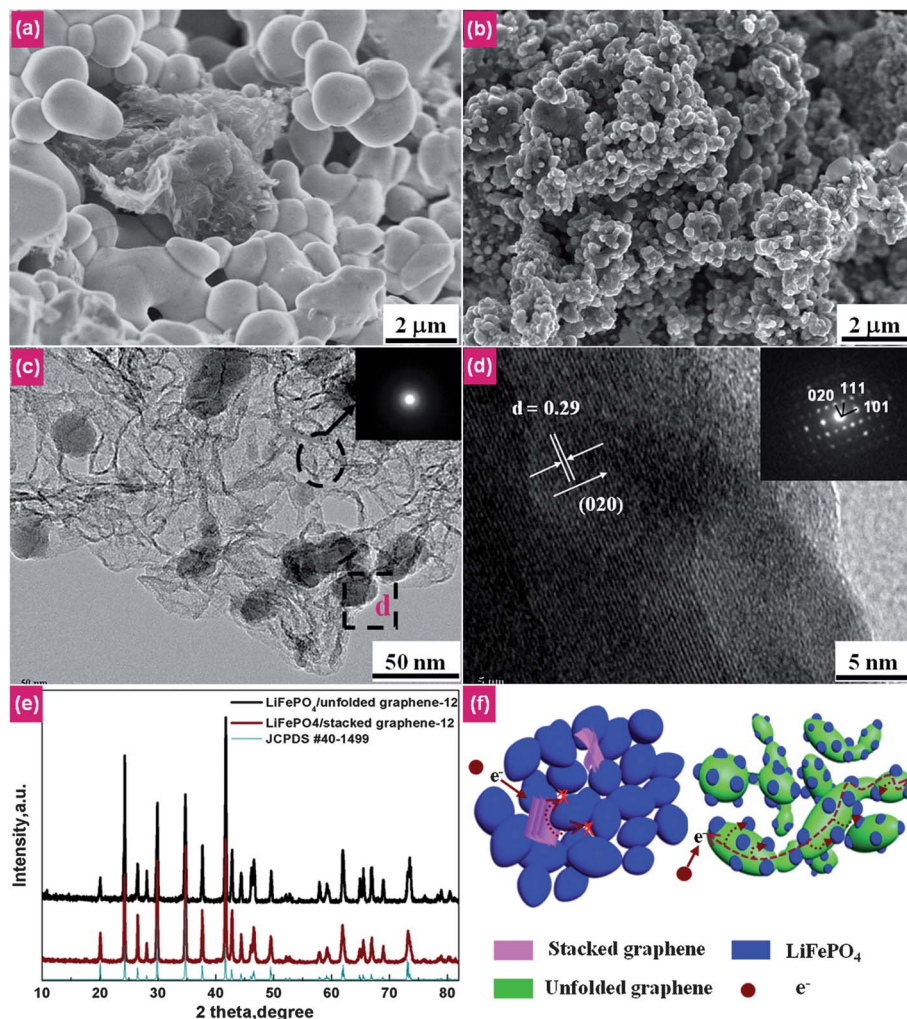
1522 | *Energy Environ. Sci.*, 2013, **6**, 1521–1528

This journal is © The Royal Society of Chemistry 2013

Fig. 2 SEM images of (a) LiFePO$_4$–stacked graphene composites and (b) LiFePO$_4$–unfolded graphene composites. (c) TEM image of LiFePO$_4$–unfolded graphene composites (inset showing the selected area electron diffraction (SAED) pattern of unfolded graphene (circle area)). (d) High-resolution TEM image and SAED pattern (inset) of an individual LiFePO$_4$ nanoparticle on unfolded graphene (square area in (c)). (e) XRD spectrum of the LiFePO$_4$–unfolded graphene and LiFePO$_4$–stacked graphene composites. (f) Electron-transfer pathway for the LiFePO$_4$–stacked graphene and LiFePO$_4$–unfolded graphene composites.

particles were attached to the stacked graphene (Fig. 2a). In contrast, many nano-scale LFP particles dispersed uniformly in the unfolded graphene network (Fig. 2b). TEM images revealed that the LFP nanoparticles in the range of 30–100 nm were firmly anchored to the unfolded graphene matrix (Fig. 2c). It should be noted that unfolded graphene provides active sites for LFP nuclei, thereby restricting the aggregation and *in situ* crystallite growth of anchored LFP nanoparticles. The HRTEM image shows the crystal lattice fringes of the LFP nanoparticles with a *d*-spacing of 0.29 nm (Fig. 2d), corresponding to the (020) plane of orthorhombic LFP crystals and indicating that the LFP nanoparticles were single crystals with high crystallinity. The selected area electron diffraction (SAED) pattern (inset of Fig. 2c) of the transparent area shows typical rings of graphene, indicating that no LFP phase exists in this region. The SAED pattern of the LFP nanoparticles (inset of Fig. 2d) indicates the single crystallinity of the LFP nanoparticles. The XRD patterns of the as-obtained LFP–SG and LFP–UG composites (Fig. 2e) demonstrated that highly pure LFP with an orthorhombic

olivine structure was successfully obtained, and no impurity phase was detected. No obvious peaks corresponding to graphene were found owing to the low graphene content. The carbon content of LFP–UG and LFP–SG composites can be calculated from the thermogravimetric (TGA) curves (see ESI, Fig. S1†). As reported, the oxidation of LiFePO$_4$ to Li$_3$Fe$_2$(PO$_4$)$_3$ and Fe$_2$O$_3$ can result in a weight gain of 5.07%.[30–32] After calculation from the TGA curves, the total weight gain for LFP–UG and LFP–SG in the TGA curve is 3.57 wt% and 3.6 wt%, respectively. Therefore, the carbon content of LFP–UG and LFP–SG is 1.5 wt% (5.07–3.57%) and 1.47 wt% (5.07–3.6%), respectively. The results demonstrate that the carbon contents of the two composites are comparable.

Fig. 2f schematically illustrates the structure of LFP–UG and LFP–SG composites. During the entire preparation process, no other carbon source except graphene was introduced. Therefore, only graphene contributes to the improvement of the electronic conductivity of LFP. In this case, the manner in which LFP and graphene are combined is crucial for the Li-ion

This journal is © The Royal Society of Chemistry 2013

Energy Environ. Sci., 2013, **6**, 1521–1528 | **1523**

intercalation and de-intercalation processes. Owing to the limited contact area between LFP and stacked graphene, the electrons can only reach certain LFP particles that are attached to the stacked graphene during the cycling process. Therefore, electrons are not able to reach LiFePO$_4$ particles from all directions (as indicated by the "×"), resulting in low utilization of LFP and polarization of the electrode.

For LFP–UG composites, the unfolded graphene acts as the conductive network, not only restricting the LFP size to nano-scale, which decreases the Li$^+$ ion diffusion path, but also enabling all of the electrons from all directions to reach all the LFP particles. The red arrows in Fig. 2f indicate that electrons can reach each of the LFP particles with the aid of the unfolded graphene. Therefore, in comparison with stacked graphene, application of unfolded graphene in electrodes can significantly enhance the utilization of the LFP.

To study the effects of annealing time on the morphology of the LFP growth on unfolded graphene, time-dependent controlled experiments were performed, as shown in Fig. 3. After 2 h of annealing (Fig. 3a), very fine LFP nanoparticles were dispersed homogenously on unfolded graphene nanosheets. As

annealing time progressed to 6 h (Fig. 3b), the nanoparticles had grown larger and were uniformly dispersed on the unfolded graphene. When the annealing time was increased to 12 h (Fig. 3c), the graphene nanosheets were crimped and connected to form a conducting 3D network, and spherical-shaped LFP nanoparticles were anchored to the graphene matrix. The nanoparticles had grown larger, with the sizes up to 100 nm. A further increase of the annealing time to 24 h (Fig. 3d), resulted in larger and irregular particles. As shown by TEM images (insets in Fig. 3a–d), with an increase in the annealing time, the particle size increased as follows: 3 nm for 2 h of annealing (LFP–UG-2), and 5 nm for 6 h of annealing (LFP–UG-6), 70 nm for 12 h of annealing (LFP–UG-12), and 200 nm for 24 h of annealing (LFP–UG-24). The results presented above reveal that the morphology and the size of the LFP nanoparticles can be tailored by adjusting the annealing time. The longer the annealing time, the larger the LFP particle size.

The successful preparation of the LFP–Graphene (LFP–G) composite was confirmed by the XRD spectrum. The XRD patterns of the LFP–G nanocomposite treated for various annealing time are shown in Fig. 4a. All of the intense peaks can
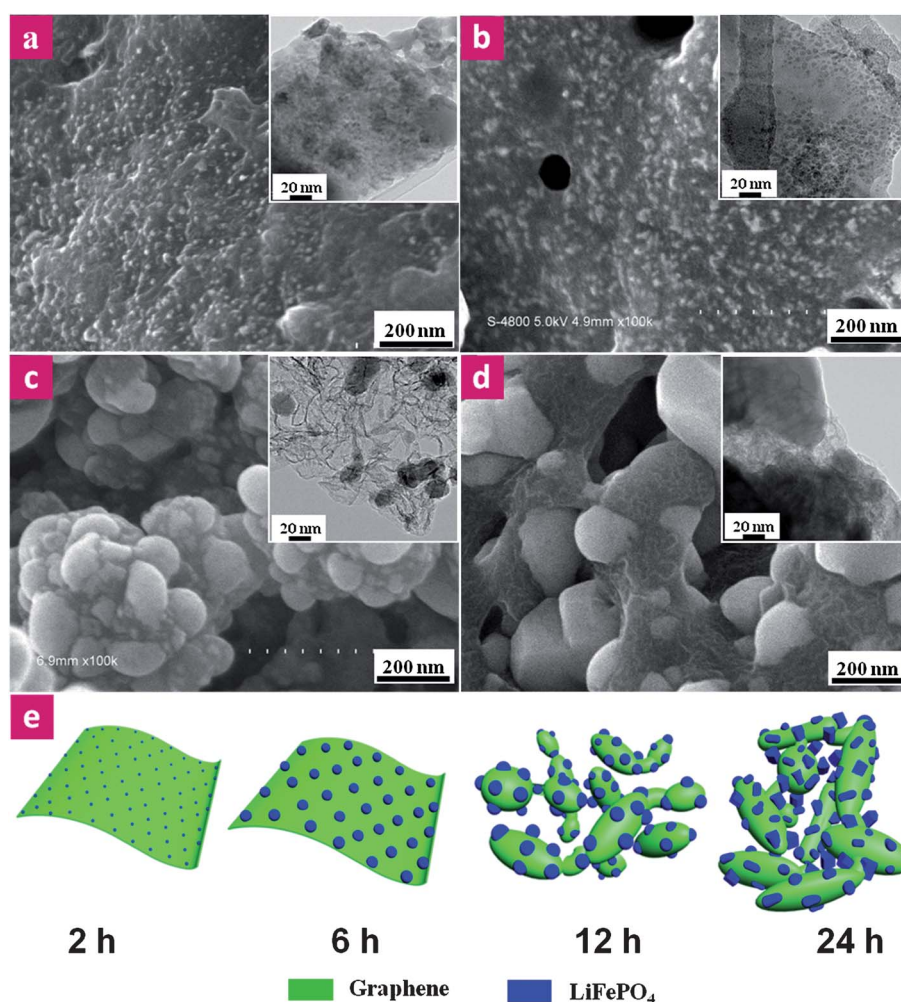

Fig. 3 SEM and TEM (inset) images of LiFePO$_4$–unfolded graphene nanocomposites obtained with different annealing time: (a) 2 h, (b) 6 h, (c) 12 h and (d) 24 h. (e) Schematic image of LiFePO$_4$ growth on the unfolded graphene.

1524 | *Energy Environ. Sci.*, 2013, **6**, 1521–1528

This journal is © The Royal Society of Chemistry 2013

be well indexed as the olivine $LiFePO_4$ phase (JCPDS Card no. 40-1499, space group Pmnb (62), $a_0 = 6.018$ Å, $b_0 = 10.34$ Å, $c_0 = 4.703$ Å), except for a small diffraction peak at 34° for the LFP–G composite annealed for 24 h, which corresponds to $Fe_7(PO_4)_6$. In addition, the crystallinity was observed to increase with the annealing time.

To further identify the effect of the annealing time effect on the crystallinity of the as-obtained products, HRTEM and SAED were conducted (see ESI, Fig. S2†). The presence of the lattice fringes indicates the single crystal nature of the nanoparticles (Fig. S2a, S2c and S2e†). The widths of the neighboring lattice fringes for LFP–UG-6 and LFP–UG-24 were 2.9 Å and 5.2 Å, respectively; these widths corresponded to the (020) and (200) planes of $LiFePO_4$, respectively. SAED spots were random (Fig. S3b†), confirming the low crystallinity of LFP–UG-2. For the LFP–UG-6 and LFP–UG-24 nanocomposites, the crystallinity gradually increased. These observations are consistent with the XRD results.

The Raman spectra of LFP–G nanocomposites are shown in Fig. 4b. Intense Raman modes were observed at 216, 282, 393, 441, 987 and 1078 cm^{-1} in three samples (LFP–UG-6, LFP–UG-12 and LFP–UG-24), corresponding to the finger print peaks of $LiFePO_4$ with orthorhombic symmetry.[33] For the LFP–UG-2 nanocomposites, there were no obvious peaks in the 200–1100 cm^{-1} region. This phenomenon is ascribed to the low crystallinity of the LFP–UG-2 composites, which is in accordance with the XRD and SAED results. The addition of graphene nanosheets had no effects on the main structure of LFP. Carbon peaks from unfolded graphene nanosheets appeared in all composites. Two strong peaks at 1342 and 1581 cm^{-1} were

assigned to the D-band and G-band, respectively. The G-band denotes the presence of the graphite carbon, whereas the D-band is attributed to disorders or defects in the graphite structure.[34] The I_D/I_G (disordered/graphitic) ratio of the Raman spectra was used to evaluate the disorder degree in the materials. With the increase of the annealing time, the I_D/I_G ratio decreased from 1.19 for LFP–UG-2 to 1.07 for LFP–UG-24. A lower I_D/I_G ratio indicates a larger amount of graphitized carbon; i.e., the amount of graphitized carbon increases with the increasing annealing time.

To investigate the chemical states and local chemistry environment of elemental Fe in the LFP–SG and LFP–UG composites and the interaction (chemical bonding) between unfolded graphene and LFP particles, Fe K-edge and C K-edge XANES spectra were collected (Fig. 4c and d). The Fe K-edge XANES spectra consist of two main edge jumps, the pre-edge and the main edge regions. The pre-edge peak was centered at the lower energy side of the sharply rising absorption edge (white line), corresponding to the 1s to 3d electronic transition of Fe.[35] As demonstrated in Fig. 4c, all of the LFP composites exhibited a distinct increased white line located at ~7126 eV, which corresponds well with the results of other groups.[35,36] For LFP–UG-2, the spectrum was broader than that of the other composites, indicating the low crystallinity of LFP–UG-2. With increasing annealing time, the spectral features became sharp, illustrating increased crystallinity of LFP–UG. The LFP–SG composites also exhibited sharp features, indicating good crystallinity. It should be noted that for LFP–UG-24 composites, the peak position of the Fe K-edge in the XANES spectrum slightly shifted toward the higher energy side. The shift in the edge position originated
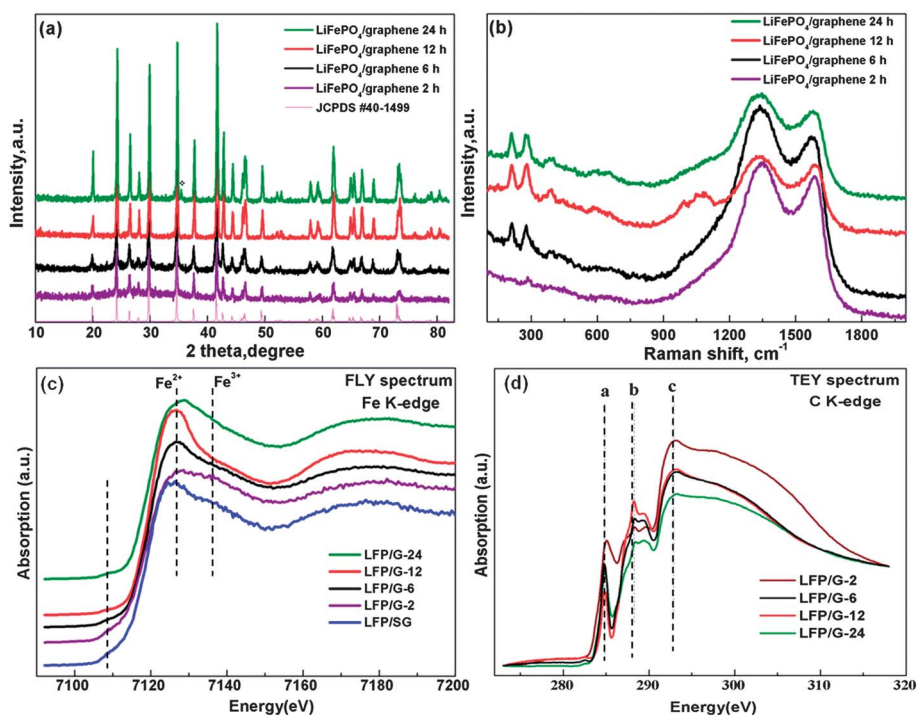

Fig. 4 XRD patterns (a), Raman spectra (b), normalized absorption of the Fe K-edge (c) and C K-edge (d) XANES spectra for $LiFePO_4$–unfolded graphene composites annealed at 700 °C for various time.

This journal is © The Royal Society of Chemistry 2013

Energy Environ. Sci., 2013, 6, 1521–1528 | 1525

from the high valence of the Fe ions, which is related to the appearance of impurity in LFP–UG-24, as shown in the XRD patterns. This shift phenomenon was also observed in Suzuki's and Yang's work.[37–39]

Two patterns in the C K-edge XANES spectra located at $\sim$285 eV and 291 eV (a and c positions) corresponded to graphitic π^* and σ^* transitions, respectively (Fig. 4d),[40] which indicated that the graphitic framework existed in all of the LFP–UG nanocomposites. Therefore good electronic conductivity in LFP–UG nanocomposites was expected. Further analysis of the XANES spectra showed several interesting features. First, π^* transition intensity (a position) for LFP–UG-12 was reduced compared with other composites. Lower intensity indicates more charge transfer from LFP to C 2p-derived π^* states in unfolded graphene,[41] indicating stronger chemical bonding between LFP and interface of unfolded graphene. Second, the intensity of resonance at $\sim$288 eV (b position) from LFP–UG-12 was stronger than the other LFP–UG composites. Many groups attribute this resonance to the chemical bonding between active materials and carboxylate groups.[41,42] The observation in the spectra further demonstrated the stronger carboxylate bonding in the LFP–UG-12 composites.

Cyclic voltammograms (CV) of LFP–UG-12 and LFP–SG composites are shown in Fig. 5a. Both electrodes exhibited a couple of redox peaks of Fe^{2+}/Fe^{3+} at a scan rate of 0.1 mV s^{-1}. For LFP–SG, the anodic peak at 3.55 V corresponded to the oxidation of Fe^{2+} to Fe^{3+}, and the reduction of Fe^{3+} to Fe^{2+} appeared at 3.29 V, where the potential interval between the two redox peaks was 0.26 V. By contrast, this interval was 0.22 V for LFP–UG-12 nanocomposites, which was approximately 40 mV smaller than that for LFP–SG composites. This difference is due

to the unfolded graphene matrix, which serves as a highly conducting 3D network that allows both Li$^+$ and electrons to migrate and reach the LFP nanoparticles that are grown on the graphene, thereby leading to efficient use of the active materials. In the subsequent cycle, the position and the currents of the two peaks were quite similar to those of the first cycle, revealing the superior stability of the LFP–UG-12 nanocomposites.

Fig. 5b shows the charge–discharge curves of the prepared LFP–SG and LFP–UG-12 composites at different cycle numbers. The cell exhibited a typical plateau at 3.41 V (versus Li$^+$/Li) associated with the Fe^{3+} to Fe^{2+} redox process for both electrodes. In the 1st cycle, the discharge capacity of LFP–UG-12 was 166.2 mA h g^{-1}, which is 98% of the theoretical capacity. The exceptionally high capacity is due to full usage of the active material. At the end of the 10th cycle and 50th cycle, the delivered capacities were 166.4 and 164.1 mA h g^{-1}, respectively, demonstrating the superior high conversion ratio of the active LFP–UG-12 material. By contrast, for LFP–SG composites, the discharge capacity was only 86 mA h g^{-1} in 50th cycle, which is approximately half that of the LFP–UG nanocomposites. As shown in the inset of Fig. 5b, the ΔE evaluated from the difference between the charge potential and the discharge potential is different for both electrodes at the 50th cycle. The polarization value was 31.4 mV and 78.8 mV for LFP–UG-12 and LFP–SG composites, respectively, which is in good agreement with the results in Fig. 4a.

The long cycling performance of LFP–UG-12 nanocomposites was investigated at a constant current density of 17 mA g^{-1}, as illustrated in Fig. 5c. No obvious decline was observed in the discharge capacity after 100 charge–discharge
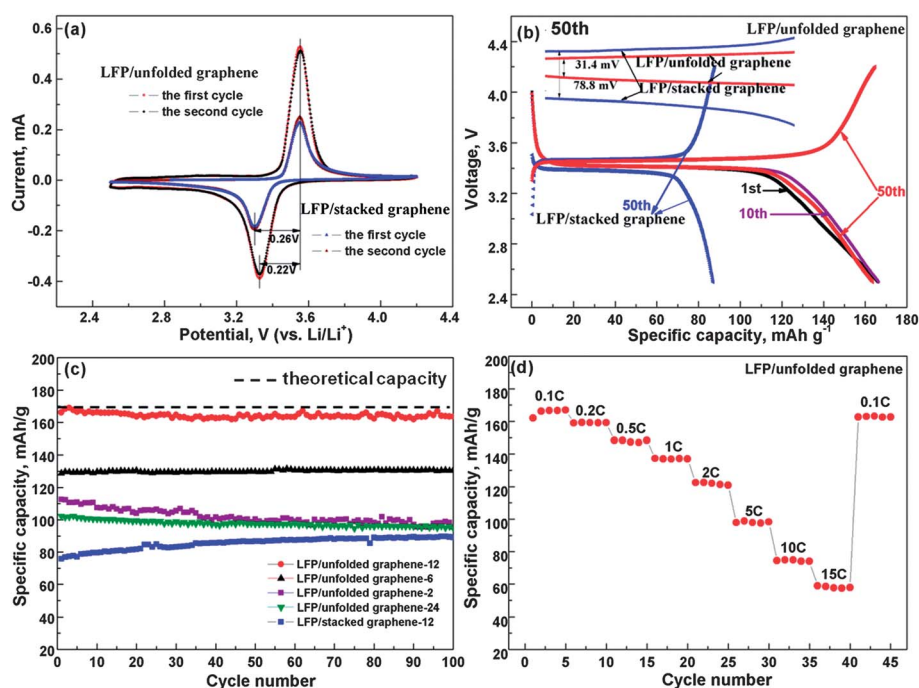

Fig. 5 (a) Cyclic voltammograms (0.1 mV s^{-1}); (b) charge–discharge curves at different cycle numbers for LFP–UG-12 and LFP–SG at a current rate of 17 mA g^{-1}; (c) cycling profiles tested at a current density of 17 mA g^{-1} between 2.5 and 4.2 V for LFP–UG and LFP–SG; (d) rate performance for LFP–UG-12.

cycles at room temperature. For example, the discharge capacity loss was less than 1.3% over 100 cycles and the coulombic efficiency was close to 100%. For comparison, the LFP–SG composites that had been annealed for the same duration were also tested at the same current density. With approximately 1.5 wt% carbon content, the LFP–SG composites also exhibited stable cycling behavior, but with low Li$^+$ storage capability as a result of insufficient usage of the active LFP material (caused by the limited contact area between LFP and stacked graphene). The products annealed for various durations were also tested. For LFP–UG-2, the capacity faded significantly at a current density of 17 mA g^{-1}. The discharge capacity in the 100th cycle was 96 mA h g^{-1}, which was only 84% of its initial capacity. Compared with LFP–UG-2, LFP–UG-6 and LFP–UG-12 exhibited better lithium intercalation/deintercalation properties. For LFP–UG-24, the initial discharge capacity delivery was 102.4 mA h g^{-1}, and a capacity fade of 6% was observed after 100 cycles. The electrochemical performance is related to the crystallinity and purity of the LFP.[43] The low crystallinity of LFP–UG-2 led to low electronic conductivity, which is apparent in the Fe K-edge XANES spectra, thereby resulting in poor lithium storage behavior. According to the HRTEM and XANES results, the crystallinity of LFP and chemical bonding between the LFP and the surface of unfolded graphene increases with an increase in the treatment duration to 12 h. Therefore, the Li$^+$ diffusion rate in the nanocomposite was improved in samples with a 6 h and 12 h annealing duration, leading to better cycle performance. However, when the annealing duration was extended to 24 h, the discharge capacity significantly decreased. The poor electrochemical performance of LFP–UG-24 can be ascribed to the presence of Fe$_7$(PO$_4$)$_6$ impurity in the nanocomposite and reduced chemical interaction between LFP and the unfolded graphene, which can be identified by the XRD patterns and XANES spectra.

The LFP–UG-12 nanocomposite was cycled at different current densities, and an excellent rate performance was observed (Fig. 5d). It should be noted that the discharge capacity of the nanocomposite remained stable at an extremely high rate of 5 C (850 mA g^{-1}, completing the discharge or charge process in 12 min), and the delivered discharge capacity was approximately 100 mA h g^{-1}. When the current density was increased to 10 C (1700 mA g^{-1}) and 15 C (2550 mA g^{-1}), the discharge capacity remained relatively high, at 75 and 60 mA h g^{-1}, respectively. It is worth mentioning that as long as the current rate was reversed back to a current density of 17 mA g^{-1}, the discharge capacity could be recovered to its original value, demonstrating that homogeneously embedded LFP nanoparticles in a superior conducting matrix can be tolerant to high charge and discharge currents, and thereby satisfying one of the mandatory electrochemical features for LIBs used in EVs and HEVs.

Conclusions

In summary, a novel nanocomposite with uniformly dispersed LFP nanoparticles anchored to an unfolded graphene matrix was developed for high-power electrode materials in LIBs. The use of an unfolded graphene matrix, which serves as a conducting 3D nano-network, enables both Li$^+$ and electrons to migrate and reach each of the LFP particles, hence realizing the full potential of the active materials. In comparison with the LFP–SG composites, the LFP–UG-12 nanocomposites delivered a much higher discharge capacity (close to the theoretical capacity) and a superior rate capability with a low graphene content of 1.5 wt%. In LFP–UG composites, the crystallinity of LFP and the chemical bonding between the LFP and unfolded graphene are improved by lengthening the annealing duration to 12 h, which can be demonstrated by XANES. The unique structure, the superior conducting properties of the graphene matrix and the strong chemical interaction between LFP and the unfolded graphene enable the LFP–UG-12 nanocomposite to achieve excellent Li storage behavior. The success of this electrode design was demonstrated by the superior characteristics of the LFP–UG nanocomposite. This design could also be extended to other cathode and anode materials, which promises to promote the development of next-generation LIBs applied in EVs and HEVs with both high-power and high-energy densities.

Acknowledgements

References

1 M. Armand and J. M. Tarascon, *Nature*, 2008, **451**, 652–657.

2 P. G. Bruce, B. Scrosati and J. M. Tarascon, *Angew. Chem., Int. Ed.*, 2008, **47**, 2930–2946.

3 Y. G. Guo, J. S. Hu and L. J. Wan, *Adv. Mater.*, 2008, **20**, 2878–2887.

4 H. Huang, S. C. Yin and L. F. Nazar, *Electrochem. Solid-State Lett.*, 2001, **4**, A170–A172.

5 A. S. Arico, P. Bruce, B. Scrosati, J. M. Tarascon and W. van Schalkwijk, *Nat. Mater.*, 2005, **4**, 366–377.

6 F. Cheng, Z. Tao, J. Liang and J. Chen, *Chem. Mater.*, 2008, **20**, 667–681.

7 A. K. Padhi, K. S. Nanjundaswamy and J. B. Goodenough, *J. Electrochem. Soc.*, 1997, **144**, 1188–1194.

8 R. Amin, P. Balaya and J. Maier, *Electrochem. Solid-State Lett.*, 2007, **10**, A13–A16.

9 S.-Y. Chung, J. T. Bloking and Y.-M. Chiang, *Nat. Mater.*, 2002, **1**, 123–128.

10 S. B. Schougaard, J. Breger, M. Jiang, C. P. Grey and J. B. Goodenough, *Adv. Mater.*, 2006, **18**, 905–909.

11 F. Croce, A. D. Epifanio, J. Hassoun, A. Deptula, T. Olczac and B. Scrosati, *Electrochem. Solid-State Lett.*, 2002, **5**, A47–A50.

12 R. Dominko, J. M. Goupil, M. Bele, M. Gaberscek, M. Remskar, D. Hanzel and J. Jamnik, *J. Electrochem. Soc.*, 2005, **152**, A858–A863.

13 R. Dominko, M. Bele, M. Gaberscek, M. Remskar, D. Hanzel, S. Pejovnik and J. Jamnik, *J. Electrochem. Soc.*, 2005, **152**, A607–A610.

This journal is © The Royal Society of Chemistry 2013

Energy Environ. Sci., 2013, **6**, 1521–1528 | **1527**

14 J. Wang and X. Sun, *Energy Environ. Sci.*, 2012, **5**, 5163–5185.

15 G. Cui, Y.-S. Hu, L. Zhi, D. Wu, I. Lieberwirth, J. Maier and K. Mullen, *Small*, 2007, **3**, 2066–2069.

16 G. Cui, L. Gu, L. Zhi, N. Kaskhedikar, P. A. van Aken, K. Mullen and J. Maier, *Adv. Mater.*, 2008, **20**, 3079–3083.

17 C. Delacourt, P. Poizot, S. Levasseur and C. Masquelier, *Electrochem. Solid-State Lett.*, 2006, **9**, A352–A355.

18 D. H. Kim and J. Kim, *Electrochem. Solid-State Lett.*, 2006, **9**, A439–A442.

19 Y. S. Hu, Y. G. Guo, R. Dominko, M. Gaberscek, J. Jamnik and J. Maier, *Adv. Mater.*, 2007, **19**, 1963–1966.

20 Y. Wang, Y. Wang, E. Hosono, K. Wang and H. Zhou, *Angew. Chem., Int. Ed.*, 2008, **47**, 7461–7465.

21 S. Park and R. S. Ruoff, *Nat. Nanotechnol.*, 2009, **4**, 217–224.

22 H. Wang, J. T. Robinson, G. Diankov and H. Dai, *J. Am. Chem. Soc.*, 2010, **132**, 3270–3271.

23 Y. Liang, H. Wang, H. S. Casalongue, Z. Chen and H. Dai, *Nano Res.*, 2010, **3**, 701–705.

24 Y. Ding, Y. Jiang, F. Xu, J. Yin, H. Ren, Q. Zhuo, Z. Long and P. Zhang, *Electrochem. Commun.*, 2010, **12**, 10–13.

25 F. Y. Su, C. H. You, Y. B. He, W. Lv, W. Cui, F. Jin, B. Li, Q. Yang and F. Kang, *J. Mater. Chem.*, 2010, **20**, 9644–9650.

26 J. Yang, J. Wang, D. Wang, X. Li, D. Geng, G. Liang, M. Gauthier, R. Li and X. Sun, *J. Power Sources*, 2012, **208**, 340–344.

27 W. S. Hummers and R. E. Offeman, *J. Am. Chem. Soc.*, 1958, **80**, 1339.

28 D. Li, M. Muller, S. Gilje, R. Kaner and G. Wallace, *Nat. Nanotechnol.*, 2008, **3**, 101–105.

29 D. Geng, Y. Chen, Y. Chen, Y. Li, R. Li, X. Sun, S. Ye and S. Knights, *Energy Environ. Sci.*, 2011, **4**, 760–764.

30 I. Belharouak, C. Johnson and K. Amine, *Electrochem. Commun.*, 2005, **7**, 983–988.

31 X. Lou and Y. Zhang, *J. Mater. Chem.*, 2011, **21**, 4156–4160.

32 J. Yang, J. Wang, X. Li, D. Wang, J. Liu, G. Liang, M. Gauthier, Y. Li, R. Li and X. Sun, *J. Mater. Chem.*, 2012, **22**, 7537–7543.

33 H. Hiura, T. W. Ebbesen, K. Tanigaki and H. Takahashi, *Chem. Phys. Lett.*, 1993, **202**, 509–512.

34 A. A. Salah, A. Mauger and K. Zaghib, *J. Electrochem. Soc.*, 2006, **153**, A1692–A1701.

35 G. X. Wang, S. Bewlay, S. A. Needham, H. K. Liu, R. S. Liu, V. A. Drozd, J. F. Lee and J. M. Chen, *J. Electrochem. Soc.*, 2006, **153**, A25–A31.

36 K. Hsu, S. Hua, C. Chen, M. Cheng, S. Tsay, T. Chou, H. Sheu, J. Lee and B. Hwang, *J. Power Sources*, 2009, **192**, 660–667.

37 K. Inoue, S. Fujieda, K. Shinoda, S. Suzuki and Y. Waseda, *Mater. Trans.*, 2010, **51**, 2220–2224.

38 X. Wang, C. Jaye, K. Nam, B. Zhang, H. Chen, J. Bai, H. Li, X. Huang, D. A. Fischer and X. Q. Yang, *J. Mater. Chem.*, 2011, **21**, 11406–11411.

39 F. Omenya, N. A. Chernova, S. Upreti, P. Y. Zavalij, K. W. Nam, X. Q. Yang and M. S. Whittingham, *Chem. Mater.*, 2011, **23**, 4733–4740.

40 J. Zhou, J. Wang, H. Fang and T. K. Sham, *J. Mater. Chem.*, 2011, **21**, 5944–5949.

41 J. Zhou, J. Wang, H. Fang, C. Wu, J. N. Cutler and T. K. Sham, *Chem. Commun.*, 2010, **46**, 2778–2780.

42 D. Wang, X. Li, J. Wang, J. Yang, D. Geng, M. Cai, R. Li, T. K. Sham and X. Sun, *J. Phys. Chem. C*, 2012, **116**, 22149–22156.

43 J. Wang, J. Yang, Y. Zhang, Y. Li, M. N. Banis, X. Li, R. Li, X. Sun, G. Liang and M. Gauthier, *Adv. Funct. Mater.*, 2013, **23**, 806–814.